Derivation of Soil Roughness Using Multi-Temporal Laser Scanning Point Clouds

Corinna HARMENING, Simone OTT, Bastian STEINHOFF-KNOPP and
Jens-André PAFFENHOLZ

Abstract

The present paper deals with the derivation of roughness parameters of soil from laser scanning point clouds, allowing to draw conclusions about properties of the soil (e. g. soil aggregation, soil sealing) and related to this its vulnerability to soil erosion. For this purpose, soil erosion scenes with agricultural cultivation are acquired in five measuring epochs under field conditions. For geo-referencing of the acquired time series of point clouds, a target-based and a data-driven approach are compared. In order to derive roughness parameters, the point clouds are cleaned of vegetation and then modelled to reduce the measurement noise. For this purpose, a collocation-based approach is used, in which a trend surface roughly approximates the point clouds. Remaining systematic deviations, which are caused by the insufficient functional approximation, are caught with the help of a stochastic signal, the variances and correlations lengths of which simultaneously provide information about the soil's roughness.

1   Introduction

Human cultivation of the ground by means of agriculture has increased the vulnerability of soils with respect to wind and water erosion. According to Germany's Welthungerhilfe, 23 % of vegetated land is considered to be permanently damaged by soil erosion, with the majority of soil erosion (60-80 %) being caused by human action. Serious consequences of soil erosion can be observed both directly on cultivated land (e. g. reduced fertility, crop failures) and apart from it (e. g. landslides, increased risk of flooding) (WELTHUNGERHILFE 2022).

The soil's vulnerability to erosion by water (erodibility) is determined by its texture, the soil's organic carbon content, rock fragments as well as its permeability (BRYAN 2000) and, thus, by the roughness of the soil surface. The soil surface's roughness is also referred to as soil microtopography (THOMSEN et al. 2015) and directly affects the surface's water storage and its infiltration capacity. Furthermore, the soil's microtopography at the millimetre to decimetre range determines the hydraulics of surface runoff and the dissipation of rain-drop energy. At the same time, it is subject to short-term changes caused by rainfall, run-off as well as transport and sedimentation of soil particles (SCHMID et al. 2012). Determining soil roughness, thus, allows risk assessment in terms of the soil's vulnerability to erosion, while monitoring the microtopography over time provides evidence of occurred erosion.

Within classical methods for the monitoring of soil erosion by water, a distinction is made between point-based strategies, with erosion pins being the most famous ones (see e. g. HAIGH 1977, ZHANG & RUTHERFURD 2020), profile-based strategies like contact profile meters (see e. g. HEGAZY 2013) and volume related strategies, which usually derive the volume by integrating the information of several profiles (STEINHOFF-KNOPP & BURKHARD 2018, ABERGEL et al. 2008). These classical strategies are usually manual and, thus, cumbersome (ABERGEL et al. 2008). Furthermore, as they require the installation of instruments within the scenes to be monitored, they are invasive (AFANA et al. 2010) and, hence, have an impact on the erosion. The measurements are either performed locally or at a multitude of measurement sites, resulting in an incomplete representation of the monitored scene (ABERGEL et al. 2008) and in laborious and time consuming measurements (SCHMID et al. 2012).

Alternatively, area-wise measurement techniques like terrestrial laser scanning (TLS) allow for a fast, efficient, contactless and large-scale data acquisition. The acquired data are of high spatial resolution and give a quasi-continuous description of the acquired scene. Due to these properties, TLS as a measurement technique outperforms the above mentioned classical strategies, as e. g. demonstrated by (THOMSEN et al. 2015) and, thus, has been established as a standard measuring technique within soil sciences (ELTNER et al. 2013).

Although the measuring technique itself is very powerful, the subsequent data analysis is usually carried out on a fairly simple level so far. Typically, the acquired laser scanning point clouds are initially rasterized to derive a digital terrain model (DTM) (see e. g. CAO et al. 2021, ELTNER & BAUMGART 2015, ASENSIO et al. 2019). By forming the differences between two DTMs, the soil loss due to erosion can be determined. However, the measured point cloud is usually directly used for these computations. A filtering of the point clouds to reduce the measurement noise, e. g. by means of a moving least squares filter (ELTNER & BAUMGART 2015) is rarely performed. Visual comparisons of the DTMs furthermore allow for broad statements regarding the change of roughness (ELTNER et al. 2013). A much more objective way to quantify soil roughness is the random roughness, which is defined as the standard deviation from points within the acquired point cloud after eliminating the slope effect, typically being realized by means of a plane estimation (ASENSIO et al. 2019, THOMSEN et al. 2015). This random roughness, however, is limited in its informative value as e. g. a planar trend surface usually only gives a very rough approximation of the soil surface and as anisotropies of the roughness cannot be taken into account. For this reason, the random roughness as a roughness measure for soil is extended for 3d point clouds captured by TLS in two ways in this paper:

- Different trend surfaces are used to eliminate deterministic effects in the 3d point clouds. Starting with planes, the trend surfaces' complexity is increased by using B-spline surfaces with an increasing number of control points. Thus, by improving the approximation quality of the trend surfaces, the soil roughness can be regarded on different scales.
- The standard deviation usually used to describe the random roughness is extended by using variograms. In this way, the roughness is considered perpendicular as well as along the trend surface. Moreover, this approach allows for the modelling of anisotropies

and, thus, the consideration of an oriented roughness.

The paper is structured as follows: Section 2 provides the methodological basics for the development of the presented approach. The data acquisition and preprocessing is described in Section 3. Section 4 introduces the extended determination of soil surface roughness, and the results yielded for the acquired data sets are analysed and evaluated in Section 5. Finally, a conclusion is drawn and an outlook is given in Section 6.

2 Spatial stochastic processes

2.1 Definitions and properties

A univariate spatial stochastic process is a collection of spatially dependent random variables $\mathscr{Z}(\mathbf{X})$, with the location in space $\mathbf{X} \in D$ varying continuously throughout the region $D \subset \mathbb{R}^3$ (CRESSIE 1993):

$$\Psi(\mathbf{X}) = \{\mathscr{Z}(\mathbf{X})\}. \tag{1}$$

A Gaussian spatial stochastic process is characterized by its first two statistical moments: its expectation value and its covariance. In case of stationarity, the expectation value μ is location invariant and the covariance $C(\mathbf{d})$ of two data points solely depends on their distance $\mathbf{d}$ in space, with $\mathbf{d}$ typically being referred to as lag vector. A spatial stochastic process is furthermore called isotropic if the covariance is direction-independent and, hence, solely depends on the absolute value d, the lag distance. As the assumption of stationarity is often not fulfilled in geostatistical applications, the weaker assumption of intrinsic stationarity (WACKERNAGEL 2003) is often used instead, stating that the variance of the differences $2\gamma(\mathbf{d})$ is location independent:

$$2\gamma(\mathbf{d}) = \text{Var}\{\mathscr{Z}(\mathbf{X}_1) - \mathscr{Z}(\mathbf{X}_2)\}, \quad \mathbf{d} = ||\mathbf{X}_2 - \mathbf{X}_1||. \tag{2}$$

$2\gamma(\mathbf{d})$ is typically referred to as (semi-)variogram.

2.2 Variogram estimation and interpretation

Assuming isotropy and a constant mean, the empirical variogram can be estimated based on the acquired data $\{\mathbf{s}(\mathbf{X})\}$ (CRESSIE 1993):

$$2\hat{\gamma}(\overline{d}_k) = \frac{1}{|N_k|} \sum_{(\mathbf{X}_{k_1}, \mathbf{X}_{k_2}) \in N_k} \left(s(\mathbf{X}_{k_1}) - s(\mathbf{X}_{k_2})\right)^2, \quad \text{with: } k_1 = 1, ..., n_l. \tag{3}$$

Equation (3) requires a subdivision of the data points' separation distances $d_{k_2,k_1} = ||\mathbf{X}_{k_2} - \mathbf{X}_{k_1}||$ into n_N consecutive intervals N_k of size $|N_k|$ with a mean lag distance $\overline{d}_k$. If the stochastic process is anisotropic, the point pairs have to be additionally grouped according to the orientation θ_{k_2,k_1} of the lag vector $\mathbf{d}_{k_2,k_1}$, resulting in directional empirical variograms. In Figure 1 (left) a typical variogram is depicted: the variance increases with increasing lag
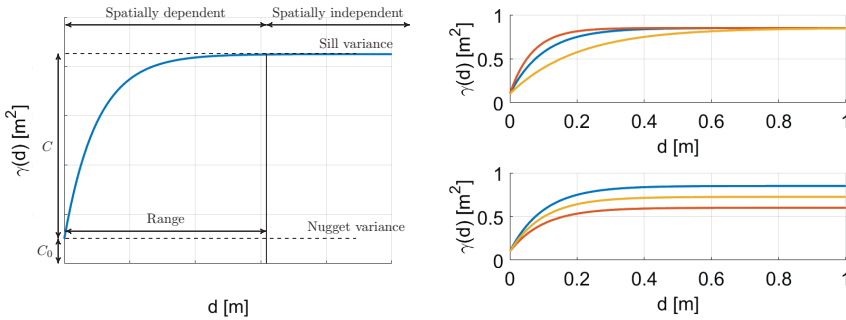
Fig. 1:   Variograms. Left: Parameters of a variogram; Right: Geometric (top) and zonal (bottom) anisotropies in directional variograms. (Directions are differentiated by colouring.) (Own illustration)

distance d, with the slope's magnitude indicating how fast the spatial dependence of point pairs decreases. The variance's convergence against an upper bound indicates second-order stationarity. The bound is denoted as *sill variance* and equals the process's variance. The lag distance after which the sill variance (or 95% of it) is reached, is denoted as the *range*. This parameter indicates the minimal distance between uncorrelated point pairs. The final variogram parameter is the *nugget variance* C_0, which is recognizable by the positive intercept between variogram and ordinate. This discontinuity is caused by an uncorrelated component, like e. g. measurement noise (OLIVER and WEBSTER 2015).

Directional variograms allow for the identification of two types of anisotropies, presented in Figure 1 (right). In the top Figure, three directional variograms converge against the same sill variance, but are characterized by different ranges (*geometric anisotropy*). Within *zonal anisotropy* (bottom Figure), the sill values vary in dependence of the variogram's direction.

3   Data acquisition and preprocessing

3.1   Field campaign

The study area is located in the southern part of Lower Saxony, Germany, near Lamspringe, at about 60 km south of Hanover. The mean annual precipitation is 800 mm, which is close to the average for Germany. Due to topsoil properties and relatively high relief energy, the area is prone to soil erosion by water. In a long-term monitoring, soil erosion is regularly mapped in semi-quantitative field surveys in this area since 2000 (STEINHOFF-KNOPP & BURKHARD 2018). In order to capture soil surface changes under real cultivation conditions, the area under investigation is situated on managed cropland.

The measurement campaign took place from 11th May 2022 to 08th June 2022 and was carried out on a weekly basis, starting immediately after sowing. Three plots, each covering
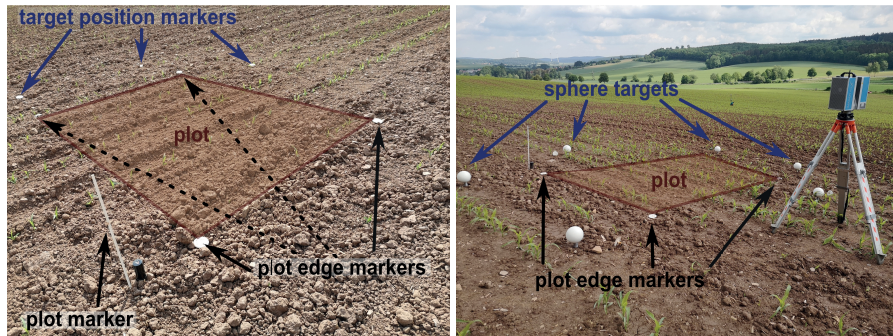
Fig. 2: Field campaign. Left: Plot setup between measurements. Right: Plot setup during scanning with TLS. Blue arrows are showing the positions of ground sleeves as target positioning markers resp. the installed sphere targets. Black arrows highlight ground sleeves marking the plot edges throughout the field campaign. (Own illustration)

2x3 m, were selected based on previously recorded erosion events considering different gradients between approx. 3 and 14 degrees in the microtopography. As most erosion events are expected at times when low soil cover coincides with heavy rainfall occurrence, the plots were placed on agricultural soil with a late sowing field crop, in this case maize.

3d point clouds were acquired from two stations in a distance of about 1 m. This measuring set-up results in a maximal incidence angle of approximately 50 degrees for each plot when assuming a plane area. Shadowing and varying incidence angles depending on the roughness of the surface were compensated by scanning from two sides of the plot. Masking of soil aggregates, tyre marks and growing vegetation lead to inhomogeneous point density which limits the transferability to a planar surface. Growing field crops lead to an increasing heterogeneity of the point density and a decline of the points representing soil surface over time. The utilized scanner Zoller+Frhlich (Z+F) IMAGER 5010X has an integrated high dynamic range camera, providing additional RGB information for the 3d point clouds.

In order to set up a stable reference coordinate system, each plot was established with six control points (CP) temporarily marked with spheres (145 mm diameter) in a distance of 1 m around the plot (see Fig. 2). The CP positions and the edges of the plot were marked by ground sleeves driven 25 cm deep into the soil, as shown in Figure 2. The ground sleeves remained during the entire field campaign, whereas the spheres were removed after each measurement epoch to avoid interference with the agricultural cultivation. In order to exclude movements of the CP, i. e. the ground sleeves, their absolute positions were observed before the weekly scanning procedure. These control measurements were conducted by means of a Trimble R8s GNSS System using an RTK-positioning with respect to a close-by SAPOS reference station and a measurement duration of 3 minutes per CP.

3.2   Geo-referencing of both stations and the acquired time series

The weekly determined CP coordinates are analysed and subsequently aggregated per CP and epoch. Within this calculation the standard deviation of this aggregation process serves as quality indicator. The standard deviation of the horizontal coordinate component is $\sigma_h \approx 6\,mm$ and the standard deviation of the vertical coordinate component is $\sigma_v \approx 12\,mm$ and thus, in the range of the RTK-GNSS accuracy for all three plots of the measurement campaign. Therefore, it can be assumed that no critical movements of the CP have occured.

The two acquired 3d point clouds per measurement epoch have to be (a) registered per epoch and (b) geo-referenced with respect to the reference coordinate system established by means of the CP. Both steps can be jointly performed by means of the CP equipped with spheres. The software Z+F LaserControl (9.3.1.33653) was used for target fitting and for the target-based registration / georeferencing. As an alternative to the target-based registration, the built-in iterative closest point (ICP) algorithm was used for registering the point clouds. As a third variant, a plane-based approach delivered by the software Scantra (Version 3.0.1.256) was applied, which jointly performs a bundle adjustment of CPs and planes to determine an optimal geo-referencing.

To compare the geo-referencing results yielded by the three approaches, the mean deviations and statistics of the CPs are considered. The registration per epoch yields a mean deviation of $0.7\,mm$ with a standard deviation of $0.3\,mm$ for the pure target-based approach. The ICP algorithm performs comparably worse with standard deviations of $\approx 6.2\,mm$ and an overlap of $\approx 60\,\%$. Thus, these results are not considered in the subsequent geo-referencing procedure. For the pure target-based geo-referencing, mean deviations of $3.9\,mm$ with a standard deviation of $1.5\,mm$ are obtained. In the plane-based approach $\approx 100 - 250$ plane identities are found to stabilise the geo-referencing. The plane identities are only established in this approach if no significant movements of the plane patches are detected. The final geo-referencing obtained from a bundle adjustment yields a standard deviation for the translation vector of each station of $2.1\,mm$ and a mean deviation of the CP of $4.2\,mm$. Thus, comparable results for the pure target-based and the plane-based approach are obtained. It can be concluded that the use of targets is essential for the subsequent analysis of 3D point cloud time series in this specific application.

3.3   Ground filtering

As the measurements were taken under field conditions, filtering is needed to remove vegetation. The ground filtering is carried out using the open source software CloudCompare (v2.12beta). Improvement of data handling and noise removal is realized by a subsampling of the 3d point cloud using voxel grid filtering with a voxel size of 1 mm. As the measurement precision is larger than the chosen voxel size, no falsification of the roughness determination is expected from this preparatory step. The homogenized 3d point cloud is levelled in order to exclude the influence of the underlying inclination on the geometric filter algorithm and to increase the comparability between both tested filter algorithms.

After levelling the 3d point cloud, the filter algorithms Cloth Simulation Filter (CSF) and

CANUPO, implemented in CloudCompare, are tested and evaluated by means of a manually cleaned reference ground surface. The CSF computes a horizontal cloth grid covering the inverted 3d point cloud surface. Afterwards, the filter algorithm compares the distances between the original 3d point cloud and the computed surface and separates the points into ground and non-ground points (see ZHANG et al. 2016). In contrast to CSF, the CANUPO algorithm is a classifier that uses point coordinates and compares the relationship of each point in the 3d point cloud to its adjacent points at multiple scales based on predefined training classes. The number of scales taken into account is one of the input settings. The more scales are set, the smaller the radius of the points considered together. These points are then categorized according to a previously created training data set. The result is a trained classifier, which can be applied on different point clouds. In its basic implementation, CANUPO considers the geometry, meaning the neighbourhood of points, as classification parameter, but there is also the possibility to include scalar fields (BRODU and LAGUE 2012). For the presented application, the best results are achieved by including RGB values rather than intensity values into the classification process as this increases the separability between living vegetation and mulch residues. Since the vegetation has grown significantly during the measurement period, each epoch contains a different amount of points representing the vegetation class. For this reason, the produced training data for the CANUPO algorithm includes vegetation and soil class of all epochs combined. Furthermore, since the population of the classes is not evenly distributed, the ratio is approximately kept the same in the training data. This reinforces the difficult process of distinguishing mulch from vegetation in epoch E_2.

Both algorithms are first carried out separately with different settings and lastly in combination using CANUPO followed by CSF, with CSF eliminating outliers yielded by CANUPO. This produces the best results, on which we focus in the following. With this procedure a substantial balanced accuracy of 0.67 for epoch E_2 is achieved, whereas epochs E_3 to E_5 even show very high balanced accuracies of above 0.91 (see table 1). Increasing green proportion in the colour index and changes in the geometrical structure of emerging vegetation in subsequent epochs may be the cause of the lower accuracy in epoch E_2 as mentioned above. Simultaneously, the larger crop height at later epochs leads to an increase in shading and, as

Table 1: Filtering performance for all epochs for an examplary plot as confusion matrix generated by comparison with a manually cleaned reference ground surface

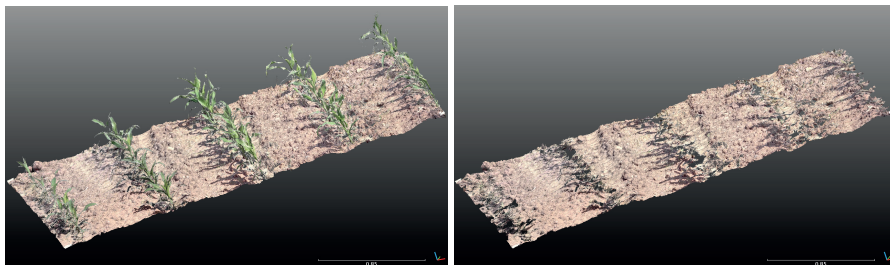|		Predicted Condition							
		Epoch E_2		**Epoch E_3**		**Epoch E_4**		**Epoch E_5**	
		P	N	P	N	P	N	P	N
Actual	P	3 131	8 799	27 403	5 672	82 588	5 655	221 859	2 560
Condition	N	24 192	1 923 922	26 951	1 719 568	59 357	1 968 993	3 824	1 667 528
Prevalence		0.01		0.02		0.04		0.12	
Prevalence Threshold		0.18		0.12		0.15		0.05	
Accuracy		0.98		0.98		0.97		1.00	
Balanced Accuracy		0.67		0.91		0.95		0.99	
Cohens' Kappa		0.15		0.62		0.91		0.98	

Fig. 3: Filtering performance in Epoch E_5. Left: Unfiltered 3d point cloud. Right: Filtered 3d point cloud using both CANUPO and CSF. (Own illustration)

a consequence, an increase in missing information in the 3d point cloud. Epoch E_5 is shown as an example in Figure 3. The ground filtering was not applied for epoch E_1 due to missing vegetation.

4   Extended determination of soil roughness

4.1   Basic considerations

The extended determination of soil roughness takes up the basic ideas of least squares collocation (LSC). Accordingly, the acquired 3d point cloud is decomposed into three parts: a deterministic trend, giving a rough approximation of the soil's surface, the stochastic measurement noise, reflecting the laser scanner's measurement uncertainties, and the stochastic signal (HEUNECKE et al. 2013). The latter is of major interest here, as it contains information about the soil surface that is not captured by the trend and, thus, provides information about the soil roughness. Following this idea, the soil roughness is interpreted to be a realization of a spatial stochastic process, which can be analysed by means of variograms. In order to illustrate this, Figure 4 presents three exemplary soil surfaces (dashed blue, solid red, dotted green) and a planar trend surface (black), which all soil surfaces vary around. The dashed
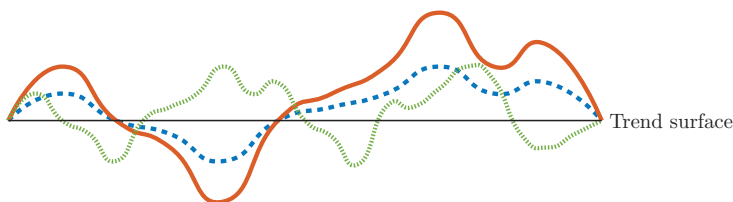

Fig. 4: Soil roughness and variogram parameters. Red (solid): Large variance, large range. Blue (dashed): Smaller variance, large range. Green (dotted): Smaller variance, smaller range. (Own illustration)

blue surface fluctuates more slowly around the planar trend than the dotted green one. This behaviour is indicated in a variogram by a larger range. The dashed blue and the solid red surface have a similar variation rate, resulting in a similar range. However, they differ in the residuals' magnitude with respect to the trend surface. This behaviour is characterized by the variogram's sill variance, which is larger for the solid red surface than for the dashed blue one. Consequently, sill variance and range can be used to describe soil roughness. However, a variogram's shape is strongly influenced by the estimated trend surface. By increasing the trend surface's complexity, both the variance and the range decrease, as the residuals' informative parts are reduced. Simultaneously, the signal's local properties emerge in the residuals.

These considerations lead to the following workflow: At first, trend surfaces with increasing complexity are estimated (section 4.2), with the simpler surfaces allowing for the modelling of global roughness properties and the more complex ones enabling the modelling of local properties. Secondly, the residuals with respect to the trend surface are analysed for anisotropies in order to detect major roughness directions (section 4.3). Finally, directional variograms are estimated and the parameters describing the soil roughness (sill variance and range) are derived (section 4.4).

4.2   Trend estimation

A planar trend is eliminated in a first step. Figure 5 (left) presents as an example the residuals v of epoch E_2 with respect to this trend. As can be seen, the planar trend gives only a rough idea about the acquired data, resulting in residuals with a magnitude of up to $8\,cm$. Additionally, the residuals' regular pattern is striking. These rills are caused by the sowing procedure. The residuals with respect to the planar trend, thus, allow for a large-scale description of the soil roughness. In order to observe the roughness on smaller scales, more complex trend surfaces are determined. For this purpose, B-spline surfaces (PIEGL & TILLER 1997) are used, the approximation quality of which can be adjusted by means of the number of estimated control points $(n_P + 1) \cdot (m_P + 1)$: The larger the number of control points, the smaller the
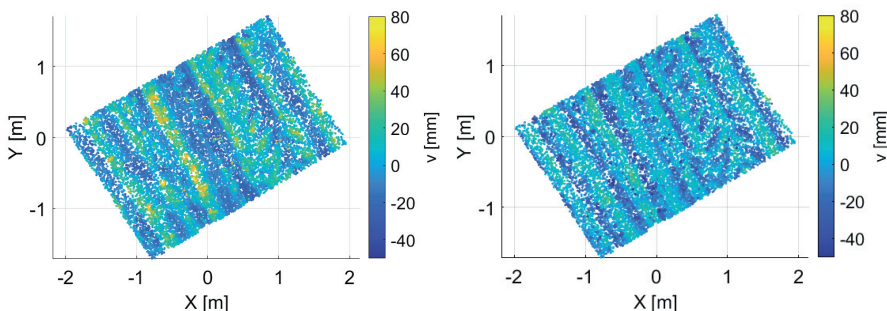

Fig. 5:   Residuals with respect to estimated trend surfaces (epoch E_2). Left: Planar trend surface. Right: B-spline surface B_2. (Own illustration)

sum of squared residuals. However, the improvement of the approximation turns into an over-fitting at a certain number of control points, which is why this parameter cannot be increased arbitrarily. In this study, three different B-spline trend surfaces are used, with the number of control points being varied from $8 \cdot 8 = 64$ (B_1) to $9 \cdot 12 = 108$ (B_2) to $10 \cdot 18 = 180$ (B_3). Figure 5 (right) presents, as an example, the residuals v of epoch E_2 with respect to B_2. As can be seen from the residuals' magnitude, this trend surface approximates the acquired data better than the planar one, resulting in residuals with a maximum magnitude of about $5\,cm$. Despite the flexible model, the pattern recognizable in Figure 5 (left) can also be observed in Figure 5 (right), albeit less extreme in the highs and lows. At the same time, new, less pronounced patterns become apparent.

4.3 Anisotropy analysis

The residuals with respect to the trend surfaces are the basis for the estimation of variograms (see section 2.2). As visible in Figure 5, the underlying stochastic process cannot be assumed to be isotropic. Thus, directional variograms are estimated, with the lag vectors' orientations θ_{k_1,k_2} being grouped into four classes $\theta_{45°} - \theta_{180°}$. A symmetry of the classes is assumed (e. g. $\theta_{45°} = \theta_{225°}$ etc.). The subscript indicates the upper bound of the respective class, meaning that i. e. class $\theta_{45°}$ contains all lag vectors with $0° < \theta_{45°} \leq 45°$ (see Fig. 6 (left) for a graphical representation). As an example, the estimated directional variograms of epoch E_2 are presented for the planar trend surface in Figure 6 (right). Three of the variograms (yellow, blue and purple) are similar in all three variogram parameters, indicating an isotropic behaviour in these three space directions. However, the red variogram, belonging to the direction $\theta_{90°}$ indicates an anisotropy. Comparing the variograms' directions with the residuals' pattern (Fig. 6, left), it becomes obvious that $\theta_{90°}$ contains the directions that run across the soils' rills. As a consequence, two directions will be considered for determining the roughness parameters: $\theta_{90°}$ as one of the major characteristic directions and $\theta_{180°}$ as the perpendicular direction which is chosen as the representative of the other directions.
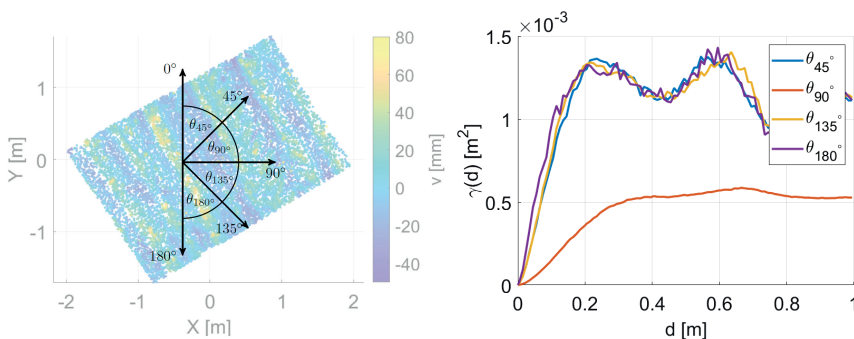

Fig. 6: Directional variograms. Left: Four classes of space vectors according to their orientation in space θ. Right: Estimated variograms for the planar trend surface (E_2). (Own illustration)

4.4   Determination of roughness parameters

Following the ideas presented in section 4.1, the variograms in directions of $\theta_{90°}$ and $\theta_{180°}$ are estimated for all four trend surfaces for all five measurement epochs $E_1 - E_5$. In order to derive the sill variance and the range, analytical variograms are fitted through the empirical ones. For this purpose, an exponential model is chosen (OLIVER & WEBSTER 2015):

$$\gamma(d) = \begin{cases} C_0 + C(1 - e^{-\frac{d}{a}}), & \text{for } d > 0 \\ 0 & \text{for } d = 0. \end{cases} \tag{4}$$

In equation (4), the parameter a denotes the range and the parameter C is the sill variance. Thus, the estimation of analytical variograms directly provides the desired roughness parameters. Occurring periodicities in the empirical variograms (cf. Fig. 6 (right)) are neglected by the exponential model. This approach is justifiable, because these periodicities reflect roughness components that are explicitly modeled in the lower-scale approaches. In the higher-scale approach, these periodicities provide information about the rills formed due to tillage and sowing. For example, for epoch E_2 it can be concluded that these rills repeat on average every 0.4 m (cf. Fig. 6 (right)).

A nugget variance C_0 is not visible in the empirical data (cf. Fig. 6 (right)) as the magnitude of the multi-scale roughness investigated in this study clearly exceeds the magnitude of the measurement noise. Therefore, a modelling of the nugget variance is neglected in this initial study. This step becomes mandatory when the roughness is investigated at a smaller scale.

5   Results

The estimated variogram parameters are presented in Figure 7. The sill standard deviation $\sqrt{C}$ (Fig. 7, left), representing the mean deviation of the soil with respect to the trend surface, slightly decreases in the direction of $\theta_{90°}$ (solid lines) over the five epochs for all four trend surfaces. Except for the last epoch, a similar behaviour can be observed in direction $\theta_{180°}$ (dashed lines). This decrease in variance indicates a decrease in roughness over time. These conclusions are confirmed by a visual analysis of the acquired soil surfaces (Fig. 8).

The variance's different behaviour in the last epoch is assumed to be caused by the vegetation, which could not be eliminated as well as in the other epochs. As a result, points representing vegetation are still present in the filtered 3d point cloud and accumulate along the planting direction $\theta_{180°}$. These outliers are incorporated in the variogram estimation and, thus, falsify the results. Comparing the variances of the two main directions, it can be concluded that the roughness along the rills is more pronounced than across them. However, it has to be taken into account that remaining vegetation may again falsify this result. As expected, the increase of the trend surfaces' complexity yields a decrease of the variance. The almost identical course of the curves belonging to the different trend surfaces shows that there are no scale-dependent variations of the roughness.

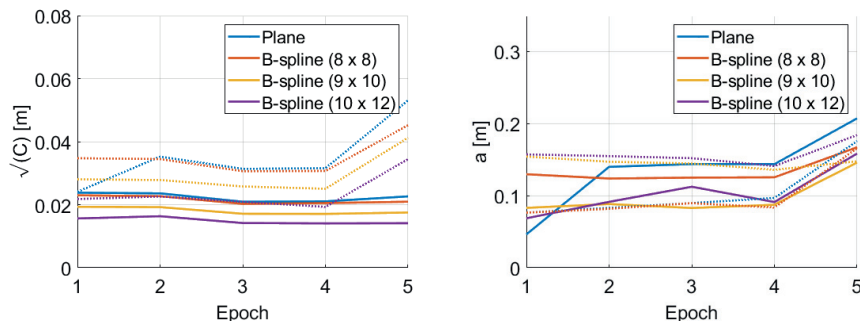The investigations have also revealed that the B-spline's tensor product representation reaches

Fig. 7: Estimated variogram parameters. Left: Sill standard deviation, right: Range. Solid lines: direction $\theta_{90°}$; dashed lines: direction $\theta_{180°}$. (Own illustration)

its limits in this application, which is characterized by very complex soil surfaces. These limits are caused by the global definition of some parameter groups (e. g. the knot vectors), which does not allow for an arbitrary improvement of the approximation quality by simply increasing the number of control points. As a consequence, an overfitting occurs in some regions, whereas other regions are not well approximated when reaching a certain complexity. These effects introduce systematics into the residuals, which directly affect the estimated variograms.

This "pseudo-roughness" can be seen in the range values a (Fig. 7, right). Although it is to be expected that systematics and, thus, correlations decrease when using more complex trend surfaces, a different behaviour is recognisable in direction $\theta_{180°}$: The curves of the more complex trend surfaces (purple and yellow) indicate a larger range than those of the simpler ones: For example, the range of the most complex B-spline surface is $a \approx 0.15\,m$, whereas the range of the plane is $a \approx 0.1\,m$ in epoch E_4. This effect is also observable for $\theta_{90°}$, although not as strongly pronounced and only for the most complex trend surface. Leaving these trend surfaces out of the interpretation, it can be seen that the ranges increase with time. This behaviour can be seen especially well for the solid blue line, which increases from $a \approx 0.05\,m$ to $0.2\,m$ from E_1 to E_5. Thus, correlations increase with time, indicating a blurrying of the soil surface over the measuring epochs. This conclusion is supported by Figure 8, showing a

Fig. 8: Photos of the soil surfaces. Left to right: Epoch E_1, E_2 and E_4. (Own illustration)

decreasing soil roughness from epoch E_1 to E_4.

Despite of the approach's potential, it is worth noting that the TLS's uncertainty and resolution limit the roughness determination: Only roughness structures in the magnitude of the measurement noise and with an extension that exceeds the measurement resolution can be detected.

6   Conclusion

In this contribution, a laser scanner-based determination of soil roughness is introduced. The approach is based on the estimation of directional variograms and, thus, takes anisotropies into account. Furthermore, it directly allows for the derivation of parameters that characterize the soil roughness. Although the parameters (sill variance and range) have a geostatistical origin, they can be related to classical roughness parameters and, therefore, can be used to draw conclusions about the soil's properties. Due to the a-priori subtraction of trend surfaces with increasing complexity, the roughness can be determined on different scales. The investigations can be used as a basis for an LSC, allowing for a filtering of the acquired soil surface which does not require a preceding rasterization. The application of the developed approach on measured data is promising. However, a variety of issues to be solved were identified:

- As remaining vegetation has proven to have a serious impact on the roughness determination, future work will focus on improving ground filter methods for point clouds.
- The anisotropy analysis conducted is realized by four arbitrarily chosen directions. Future work is going to investigate how the number and orientation of the major directions can be detected automatically.
- In order to improve the multi-scale approach, trend surfaces are required that allow for a better approximation of the complex soil surfaces. Using these trend surfaces, a modelling of the nugget variance and, thus, a separation of measurement noise and signal becomes mandatory. In this context, systematic effects of the scanner (e. g. influence of the incidence angle and penetration depth) need to be investigated.
- Finally, the results achieved with the developed methods are going to be compared with the results of classical methods.

Literatur

ABERGEL, S., FILIN, S. & GOLDSHLEGER (2008): Measurement of Erosion in Agricultural Fields Using Monoscopic Photogrammetry. Proceedings of the FIG Working Week 2008, Stockholm, Sweden, 14-19 June 2008.

AFANA, A., SOLE-BENET, A, & PEREZ, J. L. (2010): Determination of Soil Erosion Using Laser Scanners. Proceedings of the 19th World Congress of Soil Science, Brisbane, Australia, 1-6 August 2010.

ASENSIO, C., WEBER, J., LOZANO, F. & MIELNIK, L. (2019): Laser-scanner used in a wind tunnel to quantify soil erosion. In: International Agrophysics 33 (2), pp. 227-232.

BRODU, N. & LAGUE, D. (2012): 3D terrestrial lidar data classification of complex natural scenes using a multi-scale dimensionality criterion: Applications in geomorphology. In: ISPRS Journal of Photogrammetry and Remote Sensing 68, pp. 121-134.

BRYAN, R. B. (2000): Soil erodibility and processes of water erosion on hillslope. In: Geomorphology 32 (3-4), pp. 385-415.

CAO, L., WANG, Y. & LIU, C. (2021): Study of unpaved road surface erosion based on terrestrial laser scanning. In: CATENA 199.

CRESSIE, N. A. C. (1993): Statistics for Spatial Data. John Wiley & Sons, Inc.

ELTNER, A. & BAUMGART, P. (2015): Accuracy constraints of terrestrial Lidar data for soil erosion measurement: Application to a Mediterranean field plot. In: Geomorphology 245, pp. 243-254.

ELTNER, A., MULSOW, C. & MAAS, H.-G. (2013): Quantitative measurement of soil erosion fom TLS and UAV data. In: International Archives of Photogrammetry, Remote Sensing and Spatial Information Sciences XL.

HAIGH, M. J. (1977): The use of erosion pins in the study of slope evolution. Technical Bulletin 18, British Geomorphological Research Group.

HEGAZY, R. (2013): Soil Surface Profile Computation Using Portable Profile Meter with Image Processing and Tracking Technique. In: Global Journal of Researches in Engineering 13 (3).

HEUNECKE, O., KUHLMANN, H., EICHHORN, A., NEUNER, H. & WELSCH, W. (2013): Auswertung geodätischer Überwachungsmessungen. Wichmann.

OLIVER, M. A. & WEBSTER, R. (2015): Basic Steps in Geostatistics: The Variogram and Kriging. Springer International Publishing.

PIEGL, L. A. & TILLER, W. (1997): The NURBS book. Springer.

SCHMID, T., SCHACK-KIRCHNER, H. & HILDEBRAND, E. (2012): A case study of terrestrial laser scanning in erosion research: Calculation of roughness and volume balance at a logged forest site. In: International Archives of Photogrammetry, Remote Sensing and Spatial Information Sciences XXXVI, pp. 114-118.

STEINHOFF-KNOPP, B. & BURKHARD, B. (2018): Soil erosion by water in Northern Germany: long-term monitoring results from Lower Saxony. In: CATENA 165, pp. 299-309.

THOMSEN, L. M., BAARTMAN, J. E. M., BARNEVELD, R. J., STARKLOFF, T. & STOLTE, J. (2015): Soil surface roughness: comparing old and new measuring methods and application in a soil erosion model. In: SOIL 1 (1), pp. 399-410.

WACKERNAGEL, H. (2003): Multivariate Geostatistics: An Introduction with Applications. Springer.

WELTHUNGERHILFE (2022): Bodenerosion – gefährlich und unterschätzt. https://www.welthungerhilfe.de/informieren/themen/klimawandel/bodenerosion (20.09.2022).

ZHANG, W., QI, J., WAN, P.., WANG, H., XIE, D., WANG, X. & YAN, G. (2016): An Easy-to-Use Airborne LiDAR Data Filtering Method Based on Cloth Simulation. In: Remote Sensing 8 (6), p. 501.

ZHANG, N. & RUTHERFURD, I. D. (2020): The effect of instream logs on river–bank erosion: Field measurements of hydraulics and erosion rates. In: Earth Surface Processes and Landforms 45 (7), pp. 1677-1690.